RESEARCH ARTICLE

ADVANCED
ELECTRONIC
MATERIALS
Open Access
www.advelectronicmat.de

Electrospinning-Driven Binary Oxide Nanofiber Networks with Tunable Amorphous Microstructure for Booming Transistors and Circuits Operation

Bo He, Gang He,* Qingqing Hu, Shanshan Jiang, Qian Gao, Elvira Fortunato, and Rodrigo Martins

Although In_2O_3 nanofibers (NFs) are regarded as one of the active channel materials for next-generation, low-cost thin-film transistors (TFTs), these NFs-based devices still suffer from the degraded carrier mobility and operational instability, limiting the ability of such devices to replace current polycrystalline silicon technologies. Here, it is shown that nanofiber channel transistors with high electron mobility and operational stability can be achieved by selectively doping Zn element into electrospun In_2O_3 NFs. By precisely manipulating the doping level during NFs fabrication, their crystallinity, surface morphology, and corresponding device performance can be regulated reliably for enhanced transistor performances. It has been detected that $InZnO/SiO_2$ TFTs with an optimized Zn doping concentration of 50% have demonstrated the high field-effect mobility (μ_{FE}) of 6.38 cm^2 V^{-1} s^{-1}, the larger I_{ON}/I_{OFF} of 4.12×10^7 and operation in the energy-efficient enhancement-mode. Low frequency noise (LFN) measurements have displayed that the scattering and defects inside the NFs are effectively suppressed by the particular microstructure. When integrating ALD-derived Al_2O_3 films as the gate dielectric into TFTs devices, their electron mobility and I_{ON}/I_{OFF} can be further improved to 37.82 cm^2 V^{-1} s^{-1} and 2.92×10^8, respectively. To demonstrate the potential toward more complex logic applications, a low voltage resistor-loaded unipolar inverter is built by using $InZnO/Al_2O_3$ TFT, exhibiting a high gain of 20.95 and full swing characteristics. These optimized parameters have demonstrated the significant advance of this electrospinning technique toward practical applications for high performance and large-scale electronics.

1. Introduction

Due to their distinctive electron transport characteristics and exceptional optical properties, conventional metal-oxide semiconductors (MOS) have been extensively investigated and explored as the fundamental building blocks for various technological applications in photodetectors, chemical, and biological sensors, active-matrix liquid-crystal displays (AMLCDs), active-matrix organic light-emitting diode (AMOLED), and so on.[1–10] As representatives of MOS, indium oxide (In_2O_3) and zinc oxide (ZnO) have been considered as the ideal channel materials for next-generation displays and electronics, arising from their chemical stability, optical transparency, and high carrier mobility. However, the further development of these devices is still seriously hindered by the high or low electron concentration and instability.[11,12] The strategy to solve this issue is to make them exist in a multi-component form by doping, leading to improved device performance.[11–14] Based on a previous investigation, it can be noted that the mixing of two or more cations with different ionic charges and sizes is effective to make the device performance

B. He, G. He, Q. Hu, Q. Gao
School of Materials Science and Engineering
Anhui University
Hefei 230601, P. R. China
E-mail: hegang@ahu.edu.cn

The ORCID identification number(s) for the author(s) of this article can be found under https://doi.org/10.1002/aelm.202300032.

S. Jiang
School of Integration Circuits
Anhui University
Hefei 230601, P. R. China

E. Fortunato, R. Martins
Department of Materials Science/CENIMAT-I3N
Faculty of Sciences and Technology
New University of Lisbon and CEMOP-UNINOVA Campus de Caparica
2829-516 Caparica, Portugal

**ADVANCED
SCIENCE NEWS**

www.advancedsciencenews.com

**ADVANCED
ELECTRONIC
MATERIALS**

www.advelectronicmat.de

complementary, enhance the formation of an amorphous phase, and reduce the defects.[14]

Compared to two-dimensional (2D) MOS thin film materials, one-dimensional (1D) oxide semiconductor nanostructures, such as nanotubes, nanowires, and nanofiber networks (NFNs), have been widely explored as the fundamental building blocks for various technological applications owing to the size-confined physical properties and solving scaling limiting problem.[15] Among these 1D MOS candidates, NFNs as active channel layers have particularly attracted increasing attention, demonstrating with impressive characteristics in next-generation electronics. The enhanced performance in NFNs-based electronics can be attributed to the geometrical confinement provided by NFNs, which makes NFNs more competitive as the next channel materials. By far, many methods have been adopted to prepare oxide-based NFNs,[16–19] in which electrospinning is included. As a relatively promising technique, electrospinning for the preparation of NFs is widely used in the catalytic supports, multiple storage components, and photonic and electronic devices, as well as biomedical scaffolds.[15] Different from other methods that require a strict preparation environment, electrospinning is well accepted to its simplicity and versatility to yield organic, inorganic, or composite NFs. This technique can not only fabricate NFs with well-controlled properties, such as excellent crystallinity, homogeneous chemical composition, and uniform diameters but also deliver the high throughput production of NFs, which illustrates promising perspectives of deploying electrospun NFs for next-generation high-performance electronic devices.

Recently, electrospinning-driven NFNs-based oxides thin film transistors (TFTs) have been reported, such as InYbO,[9] InHfO,[20] InSrO,[21] InGaZnO,[22] and so on. In addition, these NFNs-based TFTs have displayed impressively on/off current ratios and higher field effect mobilities, which has the great potential to satisfy all the stringent requirements for practical applications in large-area, low-cost, and high-performance integrated circuits. In spite of this progress in In-based oxides TFTs, the existence of the excess carriers from the oxygen vacancies acting as the donor-like defects and the inherent surface roughness of single In-based NFNs could also seriously modulate or even deteriorate their corresponding electrical properties. Fortunately, the doping method would fit well for the electrospinning process, in which the doping concentration can be easily and precisely controlled by adjusting the composition of the starting precursor solution. Importantly, the dopant atoms/ions can also be uniformly dispersed and distributed in the obtained NFs. In this case, developing the doping process with alternative dopant elements is urgently needed. As compared with other possible dopant atoms, Zn has served as a promising dopant choice for In_2O_3 thin film material systems to act as active channel layers in TFTs.[23–25] However, precisely adjusting the doping level of the electrospun NFNs can be considered as a simple and effective approach to control their surface morphology and crystallinity for the device performance enhancement. By far, there has been no systematic survey that reports how the InZnO-TFT characteristics depend on the chemical composition ratio of the channel layer.

In this work, high-performance TFTs based on electrospun Zn-doped In_2O_3 (InZnO) NFNs were successfully fabricated by a simple electrospinning technique. Since the nonuniform size distribution of nanograins that existed within the NFNs is found to yield degraded electrical properties, we systematically assess the effect of different Zn doping level on the surface morphology, crystallinity, and electrical properties of the electrospun In_2O_3 NFNs. By precisely manipulating doping concentration during NFNs fabrication, their crystallinity, grain size distribution, surface morphology, and corresponding device performance can be regulated reliably for enhanced transistor performances. For the optimized Zn doping concentration of 50 mol%, the amorphous state and high-quality surface morphology for NFNs guarantee the impressive electrical performance of the fabricated devices, including enhanced-mode operation with a small V_{TH} of 2.8 V, a relatively high on/off current ratio of $>10^7$, a high field-effect mobility (μ_{FE}) of 6.38 cm^2 V^{-1} s^{-1}, and superior negative bias stress stability. As a key parameter for semiconductor devices in analog circuit applications, the suppressed Hooge value based on low-frequency noise (LFN) measurements were extracted to achieve the trap distribution in devices.[26,27] With the aim to further decrease the operation voltage, atomic layer deposition (ALD) derived Al_2O_3 thin film was employed as the high-κ dielectric layer for the device and the corresponding operation voltage could be substantially reduced from 40 to 3 V, while the μ_{FE} could be boosted up to 37.82 cm^2 V^{-1} s^{-1}. To prove the device's potential in more complex logic circuit applications, resistor-loaded inverter was further integrated with InZnO/Al_2O_3 TFT, demonstrating the maximum voltage gain of 20.95 and full swing characteristics. All these experimental results indicate evidently the technological application of electrospun InZnO NFNs-based TFTs for future high-performance, low-cost, and low-operating-power electronics.

2. Results and Discussion

Based on the thermogravimetric (TG) analysis (Figure S1, Supporting Information), it can be noted that all of the precursor solutions exhibit four typical thermal behavior stage and the mass remains essentially constant after 500 °C, indicating that InZnO precursor is completely transformed into InZnO metal oxide.[28a] According to the TG analysis, the annealing condition of InZnO NFNs with different molar ratios of $Zn/(Zn + In) \times 100\%$ (η_Z) can be determined to be fixed at 500 °C. Characterization from AFM has indicated that no significant difference in nanofiber diameter ($\approx$50 nm) after annealing has been detected regardless of the doping concentration (Figure S2, Supporting Information). **Figure 1**a shows the XRD patterns of InZnO fibers with different η_Z. When η_Z is less than 30%, no ZnO phase has been found except cubic bixbyite In_2O_3. With the continued increase in η_Z, wurtzite ZnO appears, especially for 60%. However, for $\eta_Z = 50\%$, the suppressed growth of all crystalline phases including In_2O_3 and ZnO has been observed. The existence of these wide humps brings InZn$_{50\%}$O closer to the amorphous structure. Indeed, the difference of the crystal structure between In_2O_3 and ZnO leads to different coordination numbers to oxygen (InO$_6$ and ZnO$_4$),[14] and these allow for the presence of an amorphous phase in InZn$_{50\%}$O. In general, in a composite system of the binary oxide compounds,
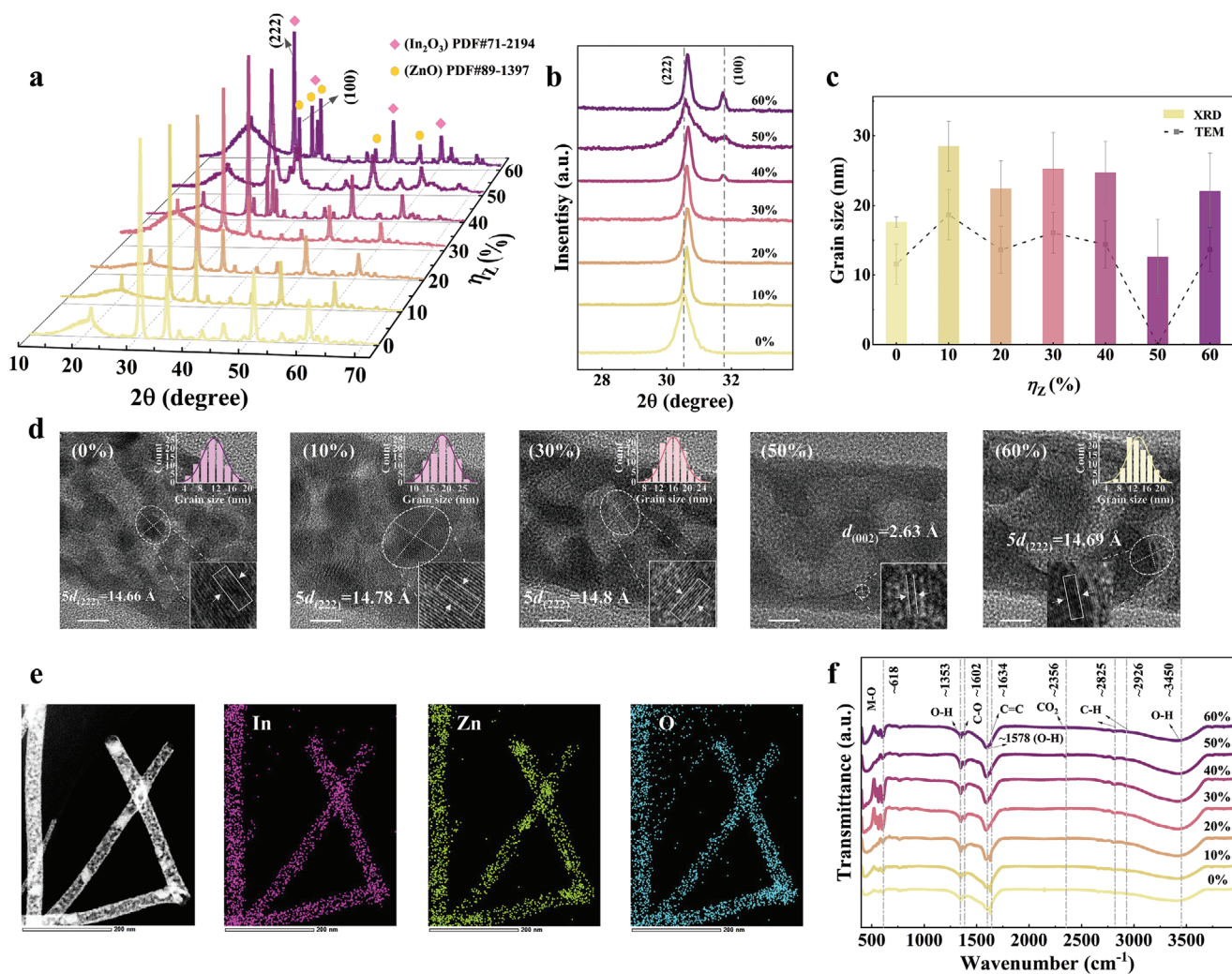
Figure 1. Characterization of the InZnO NFs. a) XRD patterns of InZnO NFs with various Zn-doping concentrations annealed at 500 °C. b) Regional XRD patterns. c) Average grain size of InZnO NFs estimated from XRD and TEM. d) HRTEM images of the annealed InZnO NFs, and the scale bar denotes 10 nm. e) Elemental mapping for In, Zn, and O of InZn$_{50\%}$O NFs. f) FTIR spectra of InZnO NFs.

a phase transition from polycrystalline to amorphous transformation occurs when the doping concentration of an element reaches a certain threshold. The mixing of two or more cations having different ionic charges and sizes is effective for enhancing the formation of an amorphous phase and suppressing crystallization.[29a] From the structural point of view of InZnO system, Zn^{2+} needs to coordinate with oxygen tetrahedral, while In^{3+} needs to coordinate with oxygen by 6, ZnO stabilizes In_2O_3 in amorphous state by preventing In octahedral relaxation and rotation from forming a thermodynamically stable cubic mangite structure. For the InZnO with a crystalline phase, the structure could be defined by mixed InO and ZnO polyhedra (bipyramids and tetrahedra) sandwiched between octahedral InO_2 planes.[29b] In the amorphous phase InZnO, local coordination motifs are usually retain, but generally appear disordered. Note that when the Zn ion is in the tetrahedral position, the In ion can hardly occupy the nearest neighbor octahedral position due to the cation charge repulsion. This implies that the region around the tetrahedron occupied by the

zinc ion is disrupted, which in turn prevents the In ion from being ordered as in the In_2O_3 crystal. According to previous reports,[29c,d] amorphous InZnO was readily formed at Zn concentrations between 40% and 60%. Moreover, the formation of amorphous is also related to the preparation method and material structure.

Namely, for our InZnO NFs system, it is entirely reasonable that InZn$_{50\%}$O demonstrates an amorphous structure. On the other side, local enlarged views (Figure 1b) demonstrate that with the increase in η_Z the characteristic peaks of the (222) and (100) crystal plane of In_2O_3 and ZnO shift to the right and the left side, respectively. The reason can be attributed to the smaller ionic radius of Zn^{2+} (0.74 Å) compared with In^{3+} (0.80 Å).[29e] The average grain size for all representative planes has been estimated as $d = \lambda/(2\sin\theta)$ and displayed in Figure 1c,[9] where λ is the incident x-ray wavelength and 2θ is the scattering angle. Except for InZn$_{50\%}$O, all the grain size is close to each other and larger than that of the pure In_2O_3, and reaches a maximum value at $\eta_Z = 10\%$. Due to the small

difference in the ionic radius of Zn^{2+} and In^{3+}, no larger lattice distortion has been observed, leading to the similar grain size in InZnO NFs. On the other hand, the incorporation of Zn^{2+} may release the stress in the fiber and promote the growth of the grain along a certain crystal plane, such as (222), and so on, resulting in the expansion and shift of the lattice.

Figure S3 (Supporting Information) shows the extracted optical band gaps of InZnO NFs and the reduced trend in band gap has been observed with the increasing η_Z, which can be attributed to the smaller band gap for ZnO compared to that of In_2O_3. In InZnO system, where the electrons are mainly transmitted by the peripheral s-orbit overlap, and the electron injection conduction band is negligible by the reduced band gap. Therefore, combining the two to will be more conducive to the separation of carriers, thus improving the electronic transmission properties, reflected by latter electrical analyses. To gain more insight into the crystal structure inside the fiber, TEM measurements were carried out. Figure 1d show HRTEM images of the InZnO NFs with different η_Z ($\eta_Z = 20\%$ and 40% are shown in Figure S4 (Supporting Information)). Unlike others that have obvious (222) crystal planes, the lattice signal

in $InZn_{50\%}O$ is very weak and almost amorphous, which is consistent with the previous XRD results. Obviously, such a special microstructure will cause differences in the device performance. The scanning transmission electron microscopy (STEM) images obtained with elemental mappings (Figure 1e) show high distribution uniformity of the elements in $InZn_{50\%}O$ fibers. The FTIR transmittance spectra of all the NFs are demonstrated in Figure 1f. The peaks associated with organics $\approx 2585\ cm^{-1}$,[30] $1634\ cm^{-1}$ and $1602\ cm^{-1}$,[30,31] can be ascribed to the vibration of C—H, C=C, and C—O groups, respectively. In addition, the vibration peaks ($<638\ cm^{-1}$) are related to the stretching vibrations of In–O and Zn–O and others.[30,32] It shows that the organic residues in the annealing fibers are essentially identical and affect the bonding of the metal atoms slightly, which provides a fair platform for comparing the electrical performance of InZnO NFN-based integrated devices.

Figure 2a,b shows the typical transfer characteristic curves and the corresponding $I_{DS}^{1/2}$ versus V_{GS} plots ($V_{DS} = 20\ V$) of the TFTs based on InZnO NFNs with different η_Z (0%, 10%, 30%, 50%, 60%), and the additional concentrations (20% and 40%) can be seen in Figure S5 (Supporting Information). $InZn_{50\%}O$
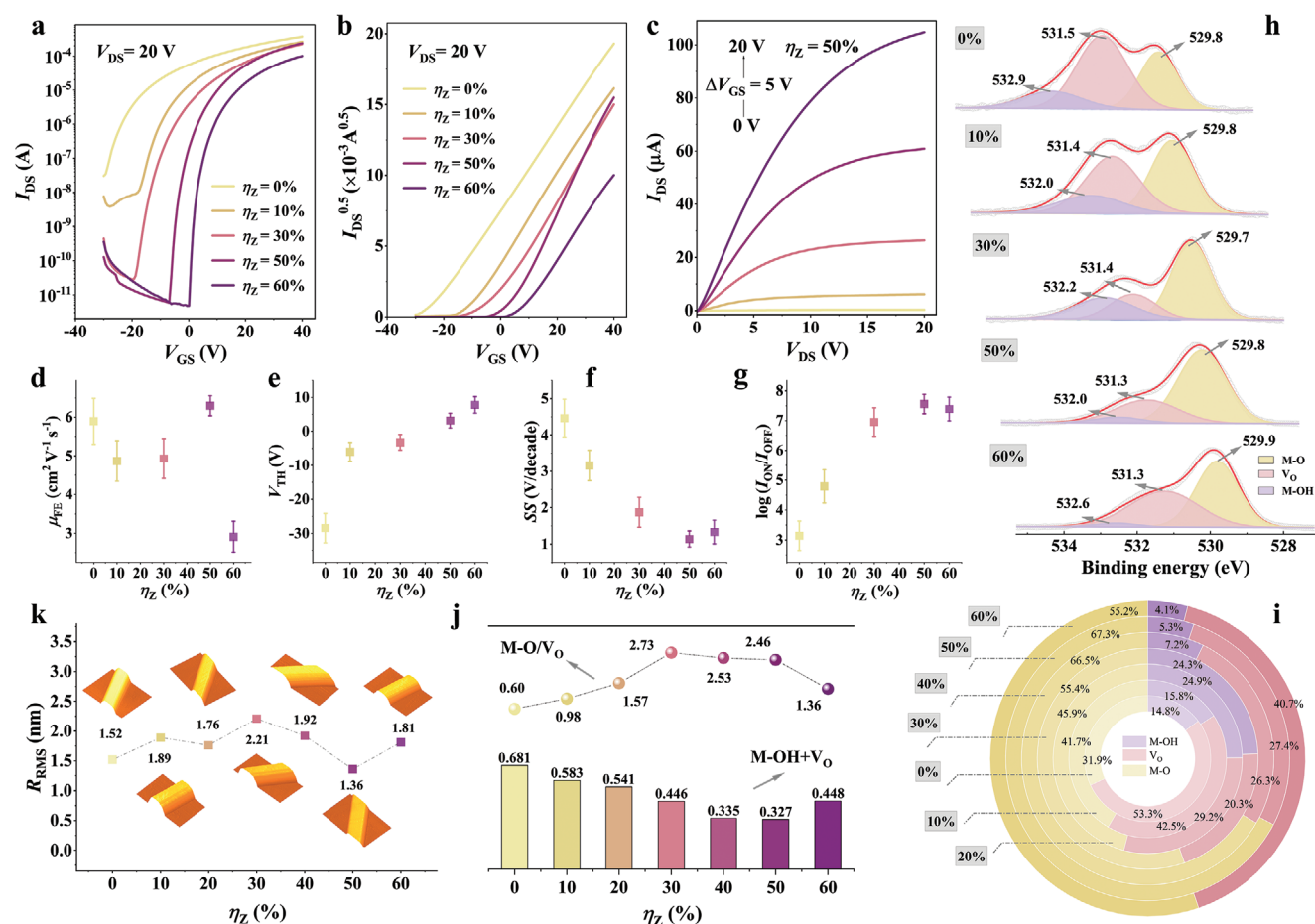
Figure 2. Characteristics and analysis of the InZnO NFN TFTs. a) Transfer characteristic and b) corresponding $I_{DS}^{1/2}$ versus V_{GS} plots ($V_{DS} = 20\ V$) for InZnO NFN TFTs with various Zn-doping concentrations of 0%, 10%, 30%, 50%, and 60%. c) Representative output characteristics of $InZn_{50\%}O$ NFN TFTs. d-g) μ_{FE}, V_{TH}, SS, and log (I_{ON}/I_{OFF}) of InZnO NFN TFTs. h) XPS spectra of O 1s for InZnO NFs. i) Semiquantitative analyses of the oxygen component of M–O, V_O, and M–OH for InZnO NFs. j) Corresponding values of M–O/V_O and M–OH+V_O for InZnO NFs. k) R_{RMS} of AFM measurement for InZnO NFs.

**ADVANCED
SCIENCE NEWS**

www.advancedsciencenews.com

**ADVANCED
ELECTRONIC
MATERIALS**

www.advelectronicmat.de

sample is selected to act as the representative output characteristic curves and shown in Figure 2c. The intuitive information from the transfer characteristic seems that the device performance improves as η_Z increases, including the forward movement of the threshold voltage (V_{TH}) and the increase of the on-state and off-state current ratios (I_{ON}/I_{OFF}). Typically, this may be attributed to the reduced free electron concentration due to doping. However, more factors should be considered for NFN TFT. Figure 2d-g shows the values of the main parameters extracted from all the devices, which follows the conventional calculation of oxide TFTs, and the detailed electrical parameters are summarized in Table S1 (Supporting Information). Except for InZn$_{50\%}$O, it can be noted that with increasing doping concentration, all the devices almost exhibit the same behavior as reported for conventional MO doping. Considering that the ZnO conductance capacity is generally weaker than In$_2$O$_3$, it is reasonable that the V_{TH} shifts forward, while the field-effect mobility (μ_{FE}) and current gradually decrease. For the abnormal performance of InZn$_{50\%}$O, including obtaining the splendid μ_{FE} of 6.38 cm^2 V^{-1} s^{-1}, the maximum I_{ON}/I_{OFF} of 4.12×10^7, the more appropriate V_{TH} of 2.8 V and SS of 1.16 V/decade, which will be discussed below. Generally, the conductivity of NFN is directly related to the fiber density, and the greater the density, the stronger the conductivity, which is also reflected in our samples, as shown in Figures S5,S6 (Supporting Information) and Table S2 (Supporting Information). It should be emphasized that, compared to In$_2$O$_3$, InZn$_{50\%}$O NFN TFTs perform better at different fiber density, which may be still depends on the amorphous structure.
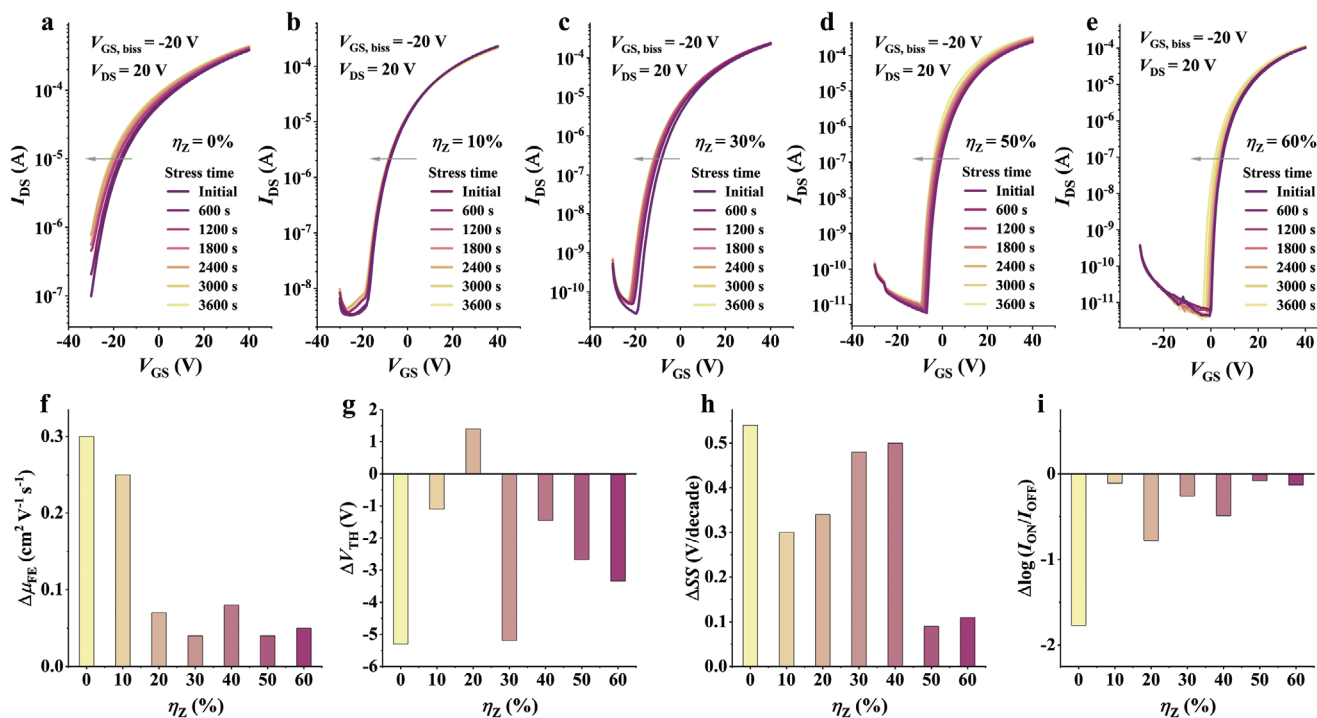
Dehuff et al. have reported that, unlike polysilicon and amorphous silicon, the magnitude of the difference in channel mobility between polycrystalline and amorphous InZnO is rather small, due to the conduction band being dominated by spherical s-orbits rather than anisotropic p- or d-orbits.[33] Actually, the disorder effect of a s-band is rather weak because its energy depends mainly on the interactions between the second adjacent metal sites, which makes the variation in the metal-metal distance the sole source of disorder. Thus, regardless of the structure, the fermi level can easily move into the conduction band, yielding a large free-carrier concentration.[34] Under these conditions, the reduction of the crystal boundary effect becomes an obvious advantage of the amorphous structure. Figure 2h and Figure S8 (20% and 40%, Supporting Information) show the chemical state of the InZnO surface detected by XPS. After the C1s peak is calibrated to 284.8 eV, the O1s peaks are divided into three peaks centered at 529.7–529.9 eV (O$_i$), 531.2–531.5 eV (O$_{ii}$) and 532.0–532.9 eV (O$_{iii}$). The peak centered at O$_i$, O$_{ii}$, and O$_{iii}$ can be assigned to the oxygen in oxide lattices (M−O), oxygen vacancy (V_o) in lattices, and oxygen in hydroxide-related (M−OH), respectively.[35,36] For all InZnO samples with different η_Z, the ratio of each oxygen peak to the sum of all peak areas is shown in Figure 2i. The M−O−M framework serves as an important electron transmission path, where a high concentration M−O−M bonding makes the electron transport more unobstructed.[36,37] The V_o can exist not only as an electron donor, but also as a capture site like M-OH.[38,39] In this way, we believe that the ratio of M−O to V_O (O$_i$/O$_{ii}$) is maintained at a right level, while the sum of V_o to M−OH (O$_{ii}$ + O$_{iii}$) values is lesser, the device performance would achieve sufficient

improvement, as in InZn$_{50\%}$O. Figure 2j summarizes the values of TFTs. Additional information related to XPS can be seen in Figure S9 (Supporting Information). The interface quality is particularly important in ultrathin electron transport channels. For electrons that rely on NFs doing linear conduction at the interface, the interface quality directly affects their scattering and capture during transport. Therefore, the exploration of the interface roughness is unavoidable. AFM images of the 3D pattern of NFs with different η_Z are shown in Figure 2k. The change trend of RMS roughness (R_{RMS}) is very dependent on the crystal situation and grain size, almost positively proportional to them. For InZn$_{50\%}$O, with the minimum R_{RMS} of 1.36 nm, the interface defects and the scattering center at the interface can be effectively reduced. In contrast, for the other devices with relatively large R_{RMS}, the SS would be pessimistic.

After obtaining better electrical performance, it is necessary to detect and evaluate the reliability of InZn$_{50\%}$O and other NFN TFTs. In general, for N-type TFTs, frequent negative bias is applied to turning-off the device. In particular, the total duration of the negative gate bias of the transistors far exceeds the positive gate bias, such as the commercial AMLCD products.[14] With these in mind, the negative gate bias stability (NBS) for all the devices was first investigated. **Figure 3**a–e and Figure S10 (η_Z = 20% and 40%, Supporting Information) show their transfer behavior under continuous negative bias for 3600 s. We think it is not accurate enough to make a judgment from the offset of V_{TH} alone, and more parameters need to be considered comprehensively (Figure 3f-i). Indeed, the ΔV_{TH} of all InZnO devices is maintained within a small and similar range.

Under the assumption that the effect of hole-trapping factors is negligible on the NFs with different η_Z,[14] the cause for the uneven variation in these parameters is most likely attributed to the environmental factors and oxygen-vacancy defects. In the bottom gate structure, the NFs with a large surface area inevitably interact with the H$_2$O in the air, leading to the release of electrons and the increased channel electron concentration.[40] Parameters that strongly depend on the electron concentration changed, such as the increased μ_{FE} and current (I_{ON} and I_{OFF}) and the negatively shifted V_{TH}. In addition, the ionization of the oxygen vacancy formed a double-ionized V_o (V_o^{2+}) also produces similar changes as described above.[41,42] These explanations seem to draw evidence from previous XPS results. As shown in Figure 2j, the proportion value of (V_o +M−OH) is the smallest in InZn$_{50\%}$O (32.7%), and the stability is even better relative to the device with a large value. The M−OH and V_o can similarly act as traps and lead to the deterioration of SS under negative gate bias. These defect states may exist in deep rather than shallow layers, as they affect the accumulated electrons before Fermi level approaches the conduction band minimum (CBM), while the μ_{FE} does not deteriorate.[42] Furthermore, the V_{TH} of InZn$_{20\%}$O exhibits a slight positive shift, which may be related to the adsorbed oxygen. In fact, the analysis part of positive gate bias stability (PBS), also proves that environmental factors dominate the reliability change of all devices (Figure S11, Supporting Information). Note that the performance of PBS for InZn$_{50\%}$O is still commendable.

To further evaluate the potential of InZnO (η_Z = 10%, 30%, 50%, and 60%) NFN-based TFTs design and application in

**ADVANCED
SCIENCE NEWS**

www.advancedsciencenews.com

**ADVANCED
ELECTRONIC
MATERIALS**

www.advelectronicmat.de

Figure 3. Bias-stress measurement of InZnO NFN TFTs. a-e) NBS ($V_{GS,\ bias} = -20$ V, $V_{DS} = 20$ V and $t = 3600$ s) for InZnO NFN TFTs with various Zn-doping concentrations of 0%, 10%, 30%, 50%, and 60%. Parameter changes of f) μ_{FE}, g) V_{TH}, h) SS, and i) log (I_{ON}/I_{OFF}) extracted from the NBS tests.

analog circuits, the low-frequency noise (LFN) properties for all the devices were investigated. The typical curves of the normalized drain current noise spectral density (S_{ID}/I^2_{DS}), taken at $V_{GS} - V_{TH} = 10$ V and $V_{DS} = 1$ V, are displayed in **Figure 4**a. By best fitting to the four S_{ID}/I^2_{DS} curves (Figure 4b-e), the extracted frequency indices γ are between 0.983 and 0.990 and all are less than 1, meaning that the traps are distributed at the interface of an insulating layer and inside the NFs above the interface.

Typically, the origins of $1/f$ noise in metal oxide TFTs have been represented by two physical noise models, namely the Hooge mobility fluctuation (HMF) model and McWhorter's carrier number fluctuation model (CNF).[26,43] The former is associated with electron–phonon scatterings, and the latter is based on the tunneling transition between the channel and the traps in the gate oxide.[26,44] Figure 4f shows the functions between over-drive gate voltage ($V_{GS} - V_{TH}$) and S_{ID}/I^2_{DS} at $f = 20$ Hz, extracted from Figure 4b–e. On the basis of the linear fitting, the slopes (k) of the TFTs with different η_Z are calculated to be −1.36, −1.39, −1.58, and −1.44, successively. Notably, except for $\eta_Z = 50\%$, the k is less than −1.5 and close to −1 at $\eta_Z = 10\%$. Here, it seems reasonable to interpret according to the HMF model, because considering the degree of crystallization of the NFs. According to the HMF model, Hooge claimed the $1/f$ noise may originate from noise in lattice scattering, which in turn causes random mobility fluctuation. Indeed, previous XRD and TEM measurements provided a good proof that InZn$_{50\%}$O NFs with close to the amorphous structure can effectively suppress the scattering of the current carrier during conduction. This somewhat weakens the defects inside the NFs, which then highlights the trap state of the interface, even when the maximum density of states (D_{it}) remains lowest (Figure 4g).

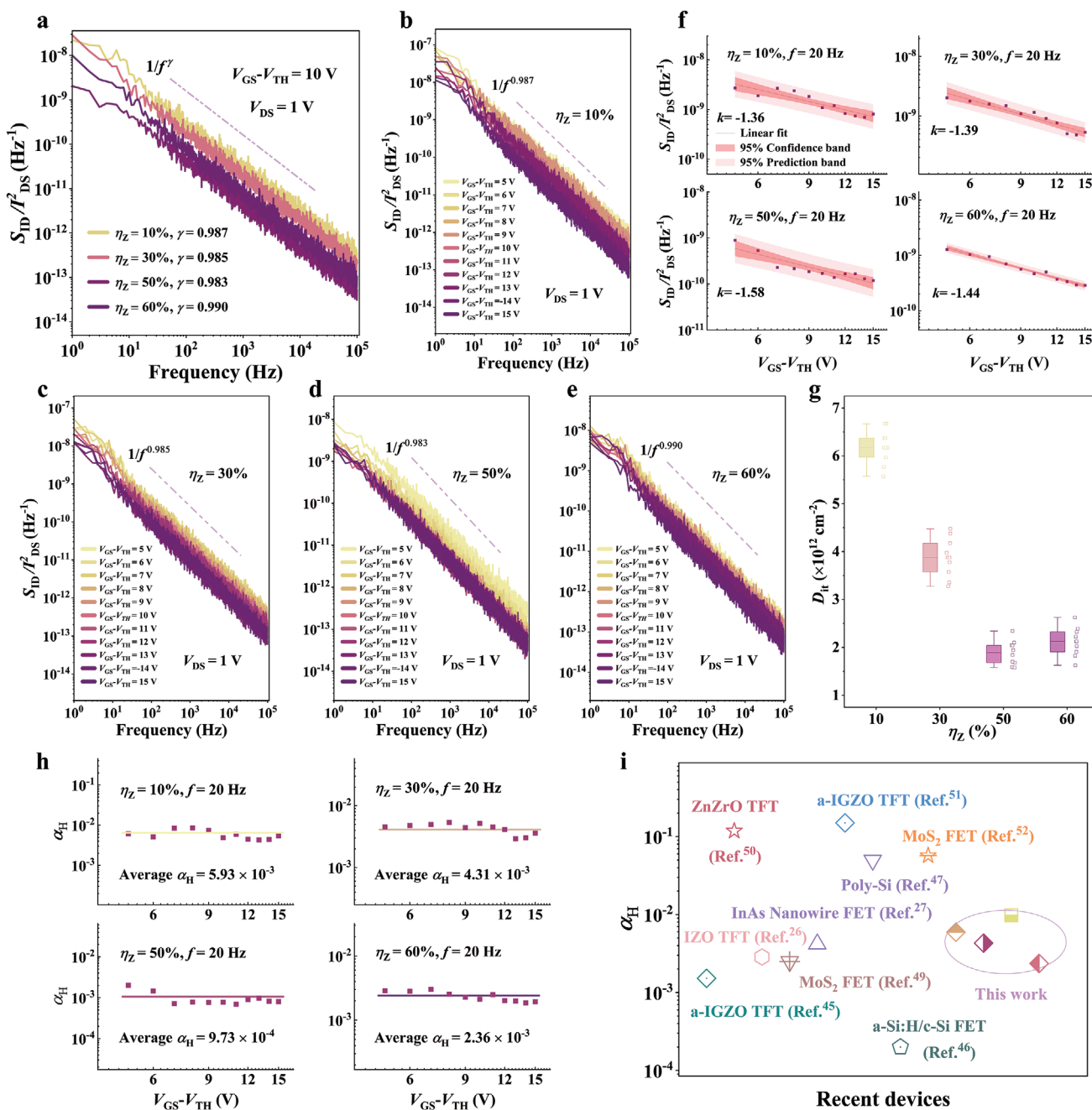In contrast, the scattering is particularly pronounced in the polycrystalline structures.

The Hooge's parameter (α_H) is frequently used as a figure of merit for the comparison of different device technologies, and its value is generally inversely proportional to the good and bad quality of the material.[45,46] We can calculate α_H from the following formula:

$$\frac{S_{ID}}{I^2_{DS}} = \frac{\alpha_H q}{f C_{ox} WL (V_{GS} - V_{TH})} \tag{1}$$

Where f is the frequency, C_{ox} is the gate oxide capacitance per unit area, q is the elementary charge, W and L are the channel length and width, respectively.[45,47]

As shown in Figure 4h, the values of average α_H are deduced to be 5.93×10^{-3}, 4.31×10^{-3}, 9.73×10^{-4} and 2.36×10^{-3}, respectively. As speculated, the reduction of nanofiber volume defects inhibits α_H, which is particularly evident in InZn$_{50\%}$O TFT with the minimum value. Similar to the amorphous properties, it may exist conduction-band tail and/or deep gap states in InZn$_{50\%}$O, but is weak relative to the effect brought by the grain boundary. Moreover, the value is not inferior to many previously found in polysilicon silicon, amorphous silicon, organic, and metal oxide transistors.[46,48] For a more intuitive comparison, Figure 4i enumerates the values reported in different materials in recent years. It is easy to observe that the α_H of our InZn$_{50\%}$O TFT is still highly competitive, and it also implies the potential in circuit applications.

Encouraged by the successful TFTs performance based on SiO$_2$ dielectric, the TFTs performance needs to be optimized to reduce the operating voltage of the device. To explore the

**ADVANCED
SCIENCE NEWS**

www.advancedsciencenews.com

**ADVANCED
ELECTRONIC
MATERIALS**

www.advelectronicmat.de

Figure 4. Low-frequency noise measurement of InZnO NFN TFTs. a) Measured normalized noise power spectral density (S_{ID}/I^2_{DS}) for InZnO NFN TFTs (η_Z = 10%, 30%, 50%, and 60%) at $V_{GS} - V_{TH}$ = 10 V and V_{DS} = 1 V. b-e) The normalized S_{ID}/I^2_{DS} as a function of frequency (f) and $V_{GS} - V_{TH}$ for different InZnO NFN TFTs. f) The normalized S_{ID}/I^2_{DS} as a function of $V_{GS} - V_{TH}$ for InZnO NFN TFTs. g) Maximum interface state density (D_{it}) extracted from transfer curves of InZnO NFN TFTs. h) Hooge's parameters (α_H) as a function of $V_{GS} - V_{TH}$ at f = 20 Hz for InZnO NFN TFTs. i) Compared to the Hooge's parameter extracted from the 1/f noise measurement for recent TFTs and FETs.[49–52]

possibility of the improvement of device performance, bottom-gated fully solution-derived TFTs combined with InZn$_{50\%}$O NFN and ALD-derived Al$_2$O$_3$ gate dielectric layer were fabricated. Figure S12 (Supporting Information) illustrates the appropriate electrical properties of Al$_2$O$_3$ film, including an area capacitance of ≈265 nF cm^{-2} at 20 Hz and a leakage current density of 4.15 × 10^{-9} A at 2.5 MV cm^{-1}. **Figure 5**a shows the schematic representation of the InZn$_{50\%}$O/Al$_2$O$_3$ NFN TFT.

The transfer characteristic curves of the selected 20 devices and representative output characteristic curves as shown in Figure 5b,c, respectively. The corresponding electrical parameters obtained from all devices at a low operating voltage of 2.5 V (Figure 5d: i–iv), including a μ_{FE} of 37.82 cm^2 V^{-1} s^{-1}, a V_{TH} of 0.49 V, a SS of 0.19 V/decade and an I_{ON}/I_{OFF} of 2.92 × 10^8. In fact, the comprehensive electrical properties exhibited by these parameters are extremely outstanding in recent studies of NFN
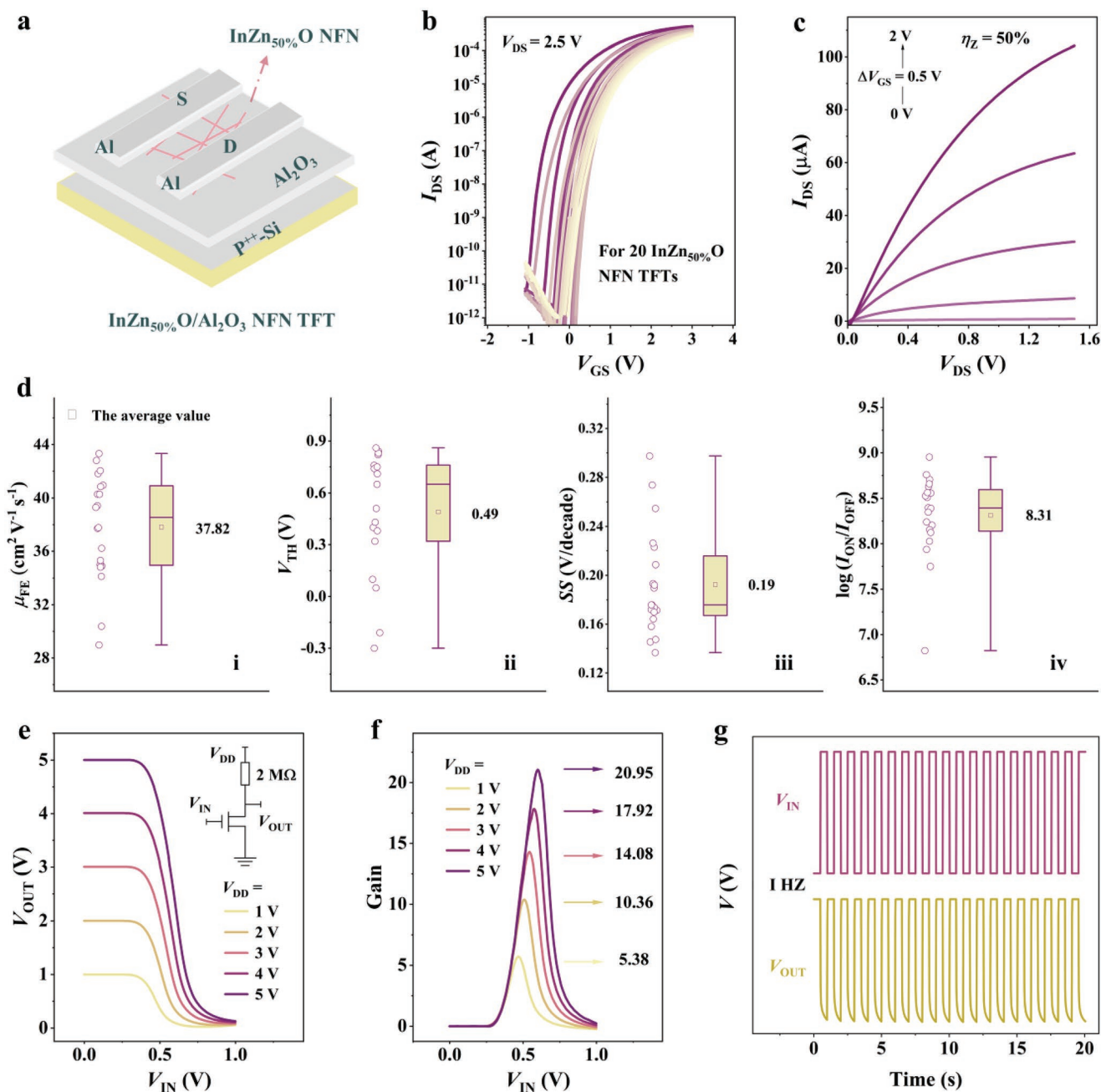
Figure 5. Electrical properties and applications of $InZn_{50\%}O/Al_2O_3$ NFN TFTs. a) Schematic of the $InZn_{50\%}O/Al_2O_3$ device architecture. b) Transfer characteristics at $V_{DS} = 2.5$ V for the 20 representative $InZn_{50\%}O$ NFN TFTs. c) Representative output characteristics of $InZn_{50\%}O$ NFN TFTs. d) Variations of μ_{FE}, V_{TH}, SS, and log (I_{ON}/I_{OFF}) evaluated from 20 $InZn_{50\%}O$ NFN TFTs. e) Voltage transfer characteristics of the inverter based on $InZn_{50\%}O$ NFN TFT. f) Corresponding gains of the inverter. g) Dynamic response behavior of the inverter under ac square waves at 1 Hz.

TFTs,[9,12,20,21,53–55] for more comparisons can be seen in Table S3 (Supporting Information).

With the excellent performance of $InZn_{50\%}O/Al_2O_3$ NFN TFTs, we moved a step further to explore the potential application in logic circuit. The typical voltage-transfer characteristics (VTCs) of the resistor-loaded inverters with a 2 MΩ external resistor based on $InZn_{50\%}O/Al_2O_3$ NFN TFTs are shown in Figure 5e, where the output high voltage is close to the supply voltages (V_{DD}), while the output low voltage is close to 0 V,

suggesting an ideal logic "1" to "0" transfer. This behavior can be attributed to the fact that $InZn_{50\%}O/Al_2O_3$ NFN TFTs have a low off-state current of TFT and good stability, and allowing the inverter can effectively convert the input voltage signal and display good full-swing characteristics.[43] Note that the gain ($-\partial V_{OUT}/\partial V_{IN}$) of 20.95 has been achieved at $V_{DD} = 5$ V (Figure 5f), indicating the unquestioned ability to drive the logic circuit components. Furthermore, Table S4 (Supporting Information) summarizes the performance of NFN TFT-based

unipolar resistor-loaded inverters reported in the literature in recent years, in which it is not difficult to find that the work is significantly better than the current inverters. As shown in Figure 5g, the dynamic response behavior under an alternative current (AC) square wave signal was measured to investigate the AC characteristic of the inverter. The output signal responds well to the input square wave signal and exhibits a little delay, implying that the inverter can achieve sufficient switching speeds. As a result, it can be concluded that $InZn_{50\%}O/Al_2O_3$ NFN TFTs with excellent electrical performance gives the potential for more complex circuit applications in the future field of applied electronics.

3. Conclusions

In conclusion, electrospinning-driven InZnO NFN TFTs with different Zn-doping concentrations have been fabricated. Among all concentration gradients, $InZn_{50\%}O$-TFT with close to the amorphous phase and high-quality surface morphology has demonstrated the optimized electrical performance, including high μ_{FE} and superior negative bias stress stability. LFN measurements have demonstrated that the noise source inside $InZn_{50\%}O$ NFs is weak, the particular amorphous structure leads to a substantial suppression of the scattering. Furthermore, the relatively ideal Hooge's parameter makes it very competitive in TFT applications. Finally, $InZnO/Al_2O_3$ TFTs were integrated. At a low operating voltage of 2.5 V, it exhibits excellent μ_{FE} of 37.82 cm^2 V^{-1} s^{-1}, high I_{ON}/I_{OFF} of 2.92×10^8, satisfied SS of 0.19 V/decade and reasonable V_{TH} of 0.49 V. The unipolar resistor-loaded inverter with high gain of 20.95 and full swing characteristics has been built based on $InZn_{50\%}O/Al_2O_3$ TFT, demonstrating potential prospects in complex logic electronics. As a result, it can be inferred that electrospinng-derived NFN will have the potential applications in constructing low-power and high-performance electronics in the future.

4. Experimental Section

Precursor Preparation: The InZnO precursor solutions with a concentration of 0.1 mol L^{-1} were prepared by indium chloride tetrahydrate ($InCl_3 \cdot 4H_2O$, 99.9%), zinc chloride ($ZnCl_2$, 99.95%) and 1.55 g of polyvinyl pyrrolidone (PVP, $M_W = 1\,300\,000$ g mol^{-1}) in 9.5 mL of N,N-dimethylformamide (DMF, 99.8%,). The molar ratios of Zn/(Zn+In) ×100% (η_Z) was 0%, 10%, 20%, 30%, 40%, 50%, and 60%, respectively. After stirring the mixture for 12 h and remaining for 2 h, a uniformly clarified precursor solution was obtained.

Dielectric and Device Fabrication: The cleaning procedure for the Si substrates followed our previous report.[28a] The cleaned Si substrates were put into the ALD equipment (MNT-ALD System) to deposit Al_2O_3 gate dielectric with thickness of 24 nm by using trimethyla-luminium [$Al(CH_3)_3$] (TMA) as the metal precursor and H_2O as the oxidant, respectively.

The typical preparation process of InZnO NFNs by electrospinning is illustrated in Figure S13 (Supporting Information). Parameters related to the electrospinning process include a needle diameter specification of 23 G, a high voltage electric field of 15 kV, a push speed of 0.4 ml h^{-1}, a distance of 15 cm and an electrospinning time of 20 s. Next, the NFNs were deposited on either Si/SiO_2 or Si/Al_2O_3 substrates, prebaked at 150 °C for 10 min, and then treated for 35 min under a UV lamp with a power of 1000 W. Finally, all the as-obtained NFNs were annealed in air for

2 h to remove excess organic matter. Based on Figure S11 (Supporting Information), it can be noted that a reduction in diameter of InZnO NFN has been observed after UV treatment and annealing. Furthermore, the nanofiber density of each InZnO NFN sample was ≈1 μm^{-1} (Figure S14, Supporting Information). Finally, Al source and drain electrodes were evaporated onto the NFN by using a shadow mask, whose channel width and length are 1000 and 200 μm, respectively.

Materials Characterization and Devices Measurement: The morphology of the NFNs was investigated by scanning electron microscopy (SEM, REGULUS 8230). The grain size and interplanar spacing of NFs were also investigated by a high-resolution transmission electron microscope (HRTEM, JEM-F200). The surface morphology and diameter of the NFNs were characterized by atomic force microscopy (AFM, 5500 M, Hitachi). X-ray diffraction (XRD, SmartLab 9 kW) was carried out to observe the crystal structure of the NFNs. The thermal behavior of InZnO precursor was investigated by a thermogravimetric analyzer (TGA, STA449F3). UV-Vis spectroscopy (UV-Vis-2550, Shimadzu) were performed to examine the optical properties of the InZnO fibers. The chemical states and functional groups of the surface were measured by x-ray photoelectron spectroscopy (XPS, ESCALAB 250Xi) and Fourier transform infrared spectroscopy (FTIR, Vertex80, Hyperion2000), respectively. The electrical properties of InZnO NFN TFTs were measured by impedance analyzer (Keithley E4990A) and semiconductor device analyzer (B1500A, Agilent; 2636B, Keithiey), respectively. The characteristic of low-frequency noise (LFN) was detected by semiconductor parameter analyzer (PDA FS-380).

The field-effect mobility (μ_{FE}) was evaluated in the linear region as follows:[28b]

$$I_{DS} = \left(\frac{WC_i\mu_{FE}}{2L}\right)/(V_{GS} - V_{TH}) \tag{2}$$

where C_i is the areal capacitance of the dielectric layer, W is the channel width, L is the channel length, V_{GS} is the gate voltage, and V_{TH} is the threshold voltage, which can be obtained in the saturation region through the maximum curvature of the $I_{DS}^{1/2}$ versus V_{GS} plot.

Supporting Information

Supporting Information is available from the Wiley Online Library or from the author.

Conflict of Interest

The authors declare no conflict of interest.

Data Availability Statement

The data that support the findings of this study are available from the corresponding author upon reasonable request.

[1] E. Fortunato, P. Barquinha, R. Martins, *Adv. Mater.* **2012**, *24*, 2945.

[2] R. S. Chen, L. F. Lan, *Nanotechnology* **2019**, *30*, 312001.

[3] J. L. Shi, J. Y. Zhang, L. Yang, M. Qu, D. C. Qi, K. H. L. Zhang, *Adv. Mater.* **2021**, *33*, 2006230.

[4] J. S. Park, W.-J. Maeng, H.-S. Kim, J.-S. Park, *Thin Solid Films* **2012**, *520*, 1679.

[5] T. Arai, *J. Soc. Inf. Disp.* **2012**, *20*,156.

[6] T. Hirao, M. Furuta, H. Furuta, T. Matsuda, T. Hiramatsu, H. Hokari, M. Yoshida, H. Ishii, M. Kakegawa, *J. Soc. Inf. Disp.* **2007**, *15*, 17.

[7] H. H. Zhu, A. Liu, K. I. Shim, H. Jung, T. Zou, Y. Reo, H. Kim, J. W. Han, Y. Chen, H. Y. Chu, J. H. Lim, H. J. Kim, S. Bai, Y. Y. Noh, *Nat. Commun.* **2022**, *13*, 1741.

[8] H. Inoue, T. Matsuzaki, S. Nagatsuka, Y. Okazaki, T. Sasaki, K. Noda, D. Matsubayashi, T. Ishizu, T. Onuki, A. Isobe, Y. Shionoiri, K. Kato, T. Okuda, J. Koyama, S. Yamazaki, *IEEE J. Solid-State Circuits* **2012**, *47*, 2258.

[9] L. Jun, Q. Chen, W. H. Fu, Y. H. Yang, W. Q. Zhu, J. H. Zhang, *ACS Appl. Mater. Interfaces* **2020**, *12*, 38425.

[10] H. H. Hsieh, H. H. Lu, H. C. Ting, C. S. Chuang, C. Y. Chen, Y. Lin, *J. Soc. Inf. Disp.* **2010**, *11*, 160.

[11] S.-H. Lee, T. Kim, J. Lee, C. Avis, J. Jang, *Appl. Phys. Lett.* **2017**, *110*, 122102.

[12] Z. Wang, Y. Meng, Y. C. Cui, C. X. Fan, G. X. Liu, B. Shin, D. J. Feng, F. K. Shan, *Nanoscale* **2018**, *10*, 14712.

[13] Y. M. Li, D. L. Zhu, W. Y. Xu, S. Han, M. Fang, W. J. Liu, P. J. Cao, Y. M. Lu, *J. Mater. Chem. C* **2020**, *8*, 310.

[14] J.-Y. Kwon, D.-J. Lee, K.-B. Kim, *Electron. Mater. Lett.* **2011**, *7*, 1.

[15] J. J. Xue, T. Wu, Y. Q. Dai, Y. N. Xia, *Chem. Rev.* **2019**, *119*, 5298.

[16] A. Aykac, I. D. Tunc, F. Gunes, M. Erol, M. Sen, *Nanotechnology* **2021**, *32*, 365501.

[17] D. Wan, A. Abliz, M. Su, C. S. Liu, C. Z. Jiang, G. L. Li, H. P. Chen, T. L. Guo, X. Q. Liu, L. Liao, *IEEE Electron Device Lett.* **2017**, *38*, 1540.

[18] G. C. Gazquez, S. Lei, A. George, H. Gullapalli, B. A. Boukamp, P. M. Ajayan, J. E. Ten Elshof, *ACS Appl. Mater. Interfaces* **2016**, *8*, 13466.

[19] H. Wu, C. Y. Hou, G. Z. Shen, T. Liu, Y. L. Shao, R. Xiao, H. Z. Wang, *Nano Res.* **2018**, *11*, 5866.

[20] Y. Meng, K. H. Lou, R. Qi, Z. D. Guo, B. Shin, G. X. Liu, F. K. Shan, *ACS Appl. Mater. Interfaces* **2018**, *10*, 20703.

[21] L. F. Song, L. Q. Luo, X. Li, D. Liu, N. Han, L. Liu, Y. B. Qin, J. C. Ho, F. Y. Wang, *Adv. Electron. Mater.* **2019**, *5*, 1800707.

[22] S. H. Choi, B. H. Jang, J. S. Park, R. Demadrille, H. L. Tuller, I. D. Kim, *ACS Nano* **2014**, *8*, 2318.

[23] B. Kumar, H. Gong, N. N. Gosvami, R. Akkipeddi, S. J. O'Shea, *Appl. Phys. Lett.* **2006**, *88*, 093111.

[24] Y. H. Kang, K. S. Jang, C. Lee, S. Y. Cho, *ACS Appl. Mater. Interfaces* **2016**, *8*, 5216.

[25] W. S. Cai, H. Y. Li, Z. G. Zang, *IEEE Electron Device Lett.* **2021**, *42*, 525.

[26] Y. Liu, H. S. He, R. Y. Chen, Y.-F. En, B. Li, Y.-Q. Chen, *IEEE J. Electron Devices Soc.* **2018**, *6*, 271.

[27] K.-M. Persson, E. Lind, A. W. Dey, C. Thelander, H. Sjoland, L.-E. Wernersson, *IEEE Electron Device Lett.* **2010**, *31*, 428.

[28] a) Y. F. Xia, G. He, W. H. Wang, Q. Gao, Y. M. Liu, *IEEE Trans. Electron Devices* **2021**, *68*, 2522; b) F. Y. Wang, L. F. Song, H. C. Zhang, Y. Meng, L. Q. Luo, Y. Xi, L. Liu, N. Han, Z. X. Yang, J. Tang, F. K. Shan, J. C. Ho, *Adv. Electron. Mater.* **2018**, *4*, 1700336.

[29] a) T. Kamiya, H. Hosono, *NPG Asia Mater.* **2010**, *2*, 15; b) A. Walsh, J. L. F. Da Silva, S.-H. Wei, *Chem. Mater.* **2009**, *21*, 5119; c) N. Itagaki, T. Iwasaki, H. Kumomi, T. Den, K. Nomura, T. Kamiya, H. Hosono, *Phys. Status Sol. A* **2008**, *205*, 1915; d) M. P. Taylor, D. W. Readey, M. F. A. M. van Hest, C. W. Teplin, J. L. Alleman, M. S. Dabney, L. M. Gedvilas, B. M. Keyes, B. To, J. D. Perkins, D. S. Ginley, *Adv. Funct. Mater.* **2008**, *18*, 3169; e) W. F. Zhang, J. S. Jie, Z. B. He, S. L. Tao, X. Fan, Y. C. Zhou, G. D. Yuan, L. B. Luo, W. J. Zhang, C.-S. Lee, S.-T. Lee, *Appl. Phys. Lett.* **2008**, *92*, 153312.

[30] C. K. Latha, M. Raghasudha, Y. Aparna, M. Ramchander, D. Ravinder, K. Jaipal, P. Veerasomaiah, D. Shridhar, *Mater. Res.* **2017**, *20*, 256.

[31] L. P. Wang, F. Zhang, *Ceram. Int.* **2017**, *43*, 9723.

[32] O. Bundit, K. Wongsaprom, *J. Phys.: Conf. Ser.* **2018**, *1144*, 012044.

[33] N. L. Dehuff, E. S. Kettenring, D. Hong, H. Q. Chiang, J. F. Wager, R. L. Hoffman, C. H. Park, D. A. Keszler, *J. Appl. Phys.* **2005**, *97*, 064505.

[34] R. Martins, P. Barquinha, I. Ferreira, L. Pereira, G. Gonçalves, E. Fortunato, *J. Appl. Phys.* **2007**, *101*, 044505.

[35] M. G. Kim, M. G. Kanatzidis, A. Facchetti, T. J. Marks, *Nat. Mater.* **2011**, *10*, 382.

[36] G. X. Liu, A. Liu, H. H. Zhu, B. Shin, E. Fortunato, R. Martins, Y. Q. Wang, F. K. Shan, *Adv. Funct. Mater.* **2015**, *25*, 2564.

[37] S. Cho, J.-H. Yang, J. G. Oh, S.-H. Cho, C.-S. Hwang, J. Jang, S. Nam, *J. Mater. Chem. C* **2017**, *5*, 6521.

[38] Y. J. Kim, S. Oh, B. S. Yang, S. J. Han, H. W. Lee, H. J. Kim, J. K. Jeong, C. S. Hwang, H. J. Kim, *ACS Appl. Mater. Interfaces* **2014**, *6*, 14026.

[39] G. M. Huang, L. Duan, G. F. Dong, D. Q. Zhang, Y. Qiu, *ACS Appl. Mater. Interfaces* **2014**, *6*, 20786.

[40] P.-T. Liu, Y.-T. Chou, L.-F. Teng, *Appl. Phys. Lett.* **2009**, *95*, 233504.

[41] W.-S. Liu, C.-L. Huang, Y.-H. Lin, C.-H. Hsu, Y.-M. Chu, *Semicond. Sci. Technol.* **2020**, *35*, 025004.

[42] M. C.-J. Ku, W.-C. Hong, T. Mohsin, R. Li, Z. Q. Duan, Y. C. Lu, *IEEE Electron Device Lett.* **2015**, *36*, 914.

[43] Y. C. Zhang, G. He, L. N. Wang, W. H. Wang, X. F. Xu, W. J. Liu, *ACS Nano* **2022**, *16*, 4961.

[44] W. E. Muhea, T. Gneiting, B. Iñiguez, *J. Appl. Phys.* **2019**, *125*, 144502.

[45] T.-C. Fung, G. Baek, J. Kanicki, *J. Appl. Phys.* **2010**, *108*, 074518.

[46] B. Hekmatshoar, *IEEE Access* **2019**, *7*, 77063.

[47] Y. Liu, S.-T. Cai, C.-Y. Han, Y.-Y. Chen, L. Wang, X.-M. Xiong, R. Chen, *IEEE J. Electron Devices Soc.* **2019**, *7*, 203.

[48] L. Jeong-Min, C. Woo-Seok, H. Chi-Sun, H. In-Tak, K. Hyuck-In, L. Jong-Ho, *IEEE Electron Device Lett.* **2009**, *30*, 505.

[49] J. Na, M. K. Joo, M. Shin, J. Huh, J. S. Kim, M. Piao, J. E. Jin, H. K. Jang, H. J. Choi, J. H. Shim, G. T. Kim, *Nanoscale* **2014**, *6*, 433.

[50] H.-C. Chiu, H.-C. Wang, Y.-C. Luo, F.-H. Huang, H.-L. Kao, K.-P. Hsueh, *Microelectron. Eng.* **2014**, *118*, 20.

[51] I.-J. Park, T. I. Kim, I.-T. Cho, C.-W. Song, J.-W. Yang, H. Park, W.-S. Cheong, S. G. Im, J.-H. Lee, S.-Y. Choi, *Nano Res.* **2017**, *11*, 274.

[52] V. K. Sangwan, H. N. Arnold, D. Jariwala, T. J. Marks, L. J. Lauhon, M. C. Hersam, *Nano Lett.* **2013**, *13*, 4351.

[53] H. C. Zhang, Y. Meng, L. F. Song, L. Q. Luo, Y. B. Qin, N. Han, Z. X. Yang, L. Liu, J. C. Ho, F. Y. Wang, *Nano Res.* **2018**, *11*, 1227.

[54] Z. D. Li, Y. Meng, C. Wang, Y. C. Cui, Z. Yao, B. C. Shin, G. X. Liu, F. K. Shan, *J. Phys. D: Appl. Phys.* **2019**, *52*, 225102.

[55] M. Belyaev, V. Putrolaynen, A. Velichko, N. Markova, *ECS J Solid State Sci Technol* **2016**, *5*, Q92.